

# The number and location of Jupiter's circumpolar cyclones explained by vorticity dynamics

Nimrod Gavriel<sup>1\*</sup> and Yohai Kaspi<sup>1</sup>

<sup>1</sup>*Department of Earth and Planetary Sciences, Weizmann Institute of Science, Rehovot, Israel*  
*\*nimrod.gavriel@weizmann.ac.il*

Preprint May 27, 2021

*Nat. Geosci.* 14, 559–563 (2021). DOI:[10.1038/s41561-021-00781-6](https://doi.org/10.1038/s41561-021-00781-6)

(Received September 7, 2020; Revised February 25, 2021; Accepted May 28, 2021)

## Abstract

The Juno mission observed that both poles of Jupiter have polar cyclones that are surrounded by a ring of circumpolar cyclones. The North Pole holds eight circumpolar cyclones and the South Pole possesses five, with both circumpolar rings positioned along latitude  $\sim 84^\circ$  N/S. Here we explain the location, stability, and number of the Jovian circumpolar cyclones by establishing the primary forces that act on them, which develop because of vorticity gradients in the background of a cyclone. In the meridional direction, the background vorticity varies owing to the planetary sphericity and the presence of the polar cyclone. In the zonal direction, the vorticity varies by the presence of adjacent cyclones in the ring. Our analysis successfully predicts the latitude and number of circumpolar cyclones for both poles, according to the size and spin of the respective polar cyclone. Moreover, the analysis successfully predicts that Jupiter can hold circumpolar cyclones while Saturn currently cannot. The match between the theory and observations implies that vortices in the polar regions of the giant planets are largely governed by barotropic dynamics, and that the movement of other vortices at high-latitudes is also driven by interaction with the background vorticity.

arXiv:2110.09422v1 [astro-ph.EP] 18 Oct 2021

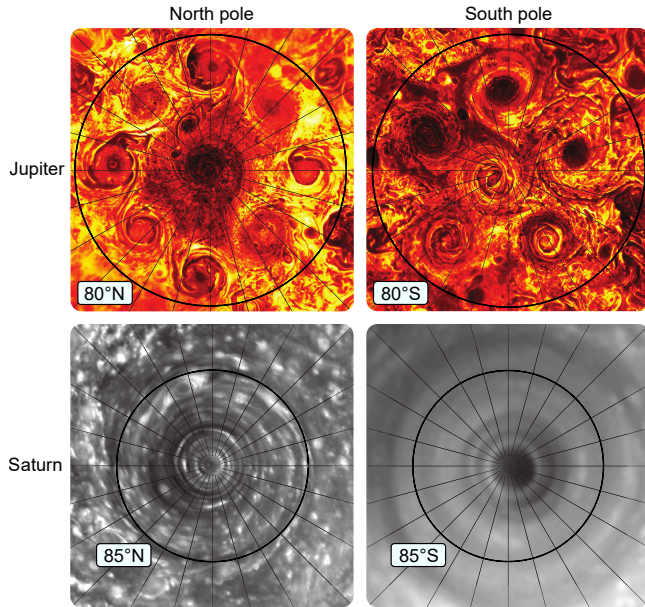


Figure 1: **Observations of the polar and circumpolar cyclones of Jupiter and Saturn.** The images of Jupiter are infrared measurements taken by Juno’s JIRAM camera<sup>3</sup> (adapted with permission). The images of Saturn were captured by the Cassini ISS<sup>9</sup> (adapted with permission). Longitude lines are pointing to the poles and are 15° apart. For Jupiter, longitude 0° in System III is positioned at the center right of the images. A latitude circle is shown at 80° N/S for Jupiter and at 85° N/S for Saturn.

The Juno orbiter entered in 2016 into a polar 53-day orbit around Jupiter<sup>1</sup> and transmitted the first-ever detailed observations of its poles<sup>2,3</sup> (Fig. 1). The images showed a unique configuration of cyclonic vortices at both poles<sup>3</sup>. Each pole contains a polar cyclone (PC) with its center positioned close to the pole and is surrounded by a ring of circumpolar cyclones (CPCs). The ring incorporates eight cyclones around the north pole and five cyclones around the south pole<sup>3</sup>. These constellations of cyclones are very stable and only drifted slightly with no substantial changes in vortex morphologies and sizes for over two years<sup>4,5</sup>. The observable diameters of the polar and circumpolar cyclones range between 4,000 and 6,000 km<sup>5</sup>, where the velocities inside the cyclones reach up to 100 ms<sup>-1</sup><sup>6</sup>. Such vortex-crystal formations were previously predicted as a 2D relaxation mechanism of turbulence and were found in experiments that simulate 2D flow with magnetized electron columns<sup>7,8</sup>. However, these configurations were never observed in nature besides at the poles of Jupiter.

Saturn is generally similar to Jupiter and displays comparable dynamics<sup>10,11,12</sup>. Both poles of Saturn also contain a central polar cyclone, each faster and more extensive than each of the Jovian PCs<sup>13</sup>. However, neither of the Saturnian

poles have an observable circumpolar ring of vortices. Any theory for the Jovian polar CPCs must also explain the absence of CPCs on Saturn.

For the poles of Jupiter, the polygonal structure of the CPCs was modeled using a single-layer shallow water (SW) model<sup>14</sup> to investigate their depth and structure and provide evidence for anticyclonic shielding around the CPCs, which was shown to be necessary to inhibit cyclone mergers. In another approach, it was shown, using deep 3D models, that Jovian cyclones could extend deep and may emanate from convection of heat<sup>15,16,17</sup> and drift poleward<sup>18,19</sup>. Such 3D vortex behavior was also studied in laboratory experiments<sup>20,21</sup>.

A primary mechanism fundamental to vortex dynamics is a secondary drift that acts on a vortex due to the sphericity of the planet<sup>22,23</sup>, and is commonly known as a “ $\beta$ -drift”. The direction of the drift is determined by the sign of the vortex and by the direction in which the background planetary vorticity rises, resulting in selective transport of cyclonic anomalies poleward while anticyclonic anomalies move equatorward. This mechanism is a major contributor to the poleward migration of tropical cyclones on Earth<sup>24,25,26,27,28</sup>. Using a 2.5-layer SW model, it was shown that moist convection, formed beneath the cloud level of a gas giant, can generate such cyclonic anomalies<sup>29,30</sup>. These, in turn, converge at the poles due to the  $\beta$ -drift and can lead to coherent PCs such as those on Saturn<sup>31,29,32</sup>. In addition to the  $\beta$ -drift, an equivalent mechanism can drive a vortex by the presence of any background vorticity gradient. For example, this gradient can be induced by jet streams and influence the movement of a crossing vortex<sup>33,34</sup>. This generalization appears to be crucial for understanding the stability of the circumpolar vortices on Jupiter.

### Vortex drift by a background vorticity gradient

For understanding the stability of the CPCs, it is essential to generalize the beta-drift as a force that acts in the direction of rising background vorticity. For intuition, one can think of a simplistic scenario in which the conserved potential vorticity (PV) is a superposition of constant vorticity by a solid disk, counter-clockwise rotating vortex, and of an unspecified background vorticity ( $\omega$  in Fig. 2) that monotonically rises northward. A fluid parcel that starts on the southern edge of the vortex, where background vorticity is small, will be carried by the vortex circulation to the eastern edge, where background vorticity is higher (Fig. 2a). To conserve PV, negative relative vorticity would be induced. The opposite will happen with a northern parcel that will induce positive vorticity while reaching the west side. This dipole of induced vorticity, usually termed “ $\beta$ -gyres”<sup>35,36</sup>, will then shear the velocity field and thus generate a northward velocity profile (Fig. 2b). The mean force acting on a vortex due to this phenomenon is proportional to the gradient of background vorticity both in magnitude and in direction. Counter-clockwise rotating vor-

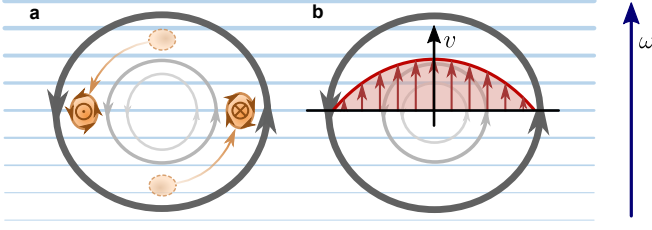


Figure 2: **Beta-drift schematic.** Gray contours represent streamlines of a vortex. Blue contours represent lines of equal background vorticity ( $\omega$ ), where their increasing thickness represents the gradual increase in the magnitude of the background vorticity. **a**, The Lagrangian motion of two fluid parcels leads to a dipole of induced vorticity due to the conservation of PV during the motion led by the vortex. **b**, A velocity profile induced in the vortex by the shearing due to the vorticity dipole illustrated in **a**.

tices are pulled toward the highest ascent of background vorticity, while clockwise rotating vortices are pulled toward the highest descent. In the planetary context (considering  $\omega$  as the planetary vorticity), this results in cyclones being pulled poleward and anticyclones equatorward.

### Meridional stability of circumpolar cyclones

If the only vorticity gradient present in the background of a cyclone is due to the planetary sphericity, it will tend to move poleward until this gradient vanishes precisely at the pole. Assuming a PC is already present at the pole (Fig. 3), the PC will induce a vorticity gradient of itself around the pole. The velocity profiles observed for the PCs of Jupiter and Saturn resemble a solid-disk rotation in an inner region, and an exponential decay outside of it (Extended Data Figs. 1 and 2). Where velocity decays exponentially, relative vorticity is negative due to the functional relation between velocity and vorticity (Methods, Extended Data Fig. 3). As the vorticity of the PC must vanish far away, an annulus of positive relative vorticity gradient should exist around a PC due to its presence. However,  $f$  has its maximum magnitude at the poles and is 0 at the equator. Therefore, its gradient ( $\beta \equiv \frac{\partial f}{\partial r}$ ) is always negative away from the pole. The magnitude of  $\beta$  is highest near the equator and vanishes at the poles<sup>37</sup>. These trends mean that theoretically, there can be a latitude where a poleward migrating CPC will be in equilibrium since the gradients of vorticity due to the PC and due to the planetary sphericity are equal and opposite<sup>14</sup>. We propose this criterion of whether a PC can generate a vorticity gradient that opposes  $\beta$  as a separating threshold between two polar states: one state in which a circumpolar ring of vortices can be stably held, and one in which the planetary gradient of vorticity is always greater, where any incoming CPC will be merged into the PC.

Considering the meridional balance on a CPC, we define

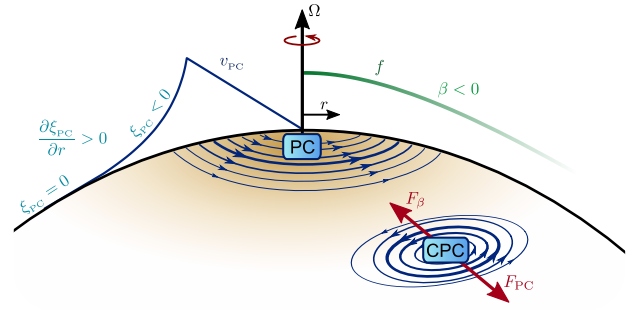


Figure 3: **An illustration of the balance holding a circumpolar cyclone (CPC) around the polar cyclone (PC).**  $r$  is the distance from the pole (note that  $r$  defines the positive meridional direction of gradients). The green curve is the vertical component of the planetary vorticity  $f$ . The blue curve is the profile around the PC of the idealized axisymmetric tangential velocity in the vortex ( $v_{PC}$ ).  $\xi_{PC}$  is the relative vorticity due to the presence of the PC.  $\Omega$  is the planetary rotation rate. The red arrows are vorticity gradient forces on the CPC, induced by the PC and by planetary sphericity.

$$F_{\theta} \equiv \frac{\partial \xi_{PC}}{\partial r} + \beta, \quad (1)$$

which is proportional to the net meridional force on a CPC ( $F_{PC} - F_{\beta}$  in Fig. 3). It is required that  $F_{\theta} = 0$  for a CPC to be in a meridional balance. Moreover, if  $F_{\theta}$  is negative, the force is in the poleward direction; positive  $F_{\theta}$  pushes cyclones equatorward. In Fig. 4a,  $F_{\theta}$  is plotted as a function of latitude. The four curves are drawn according to relative vorticity gradients calculated from idealized profiles of the PCs' tangential velocity (Methods). These profiles are determined according to the maximum velocities and the radii of maximum velocity evaluated for the respective PCs on the north and south poles of Jupiter and Saturn<sup>6,13</sup> (Methods). Temporal and local variations of the velocity fields are not taken into account. The  $\beta$  profiles are calculated according to the respective planetary radii and rotation rates of Jupiter and Saturn (Methods).

It is evident (Fig. 4a) that both poles of Saturn cannot sustain a meridional equilibrium, and therefore do not have CPCs. In contrast, each pole of Jupiter exhibits two equilibrium points. However, the equilibrium point closer to the pole (in each of the red curves) is unstable. This is because a perturbation in the latitude of the CPC poleward from that point will further pull it to merge with the PC due to the negative vorticity gradient poleward of that point. A perturbation away from the pole will bring the vortex to the farther point of equilibrium. That point is in stable equilibrium, situated at latitude  $\sim 84^{\circ}$  for both poles. The circumpolar ring observed at J-NP lies approximately along  $83^{\circ}$ N, while at J-SP, it is roughly at  $84^{\circ}$ S<sup>4</sup>. This agreement between the calculated latitudes of equilibrium (Fig. 4) and observations and the lack

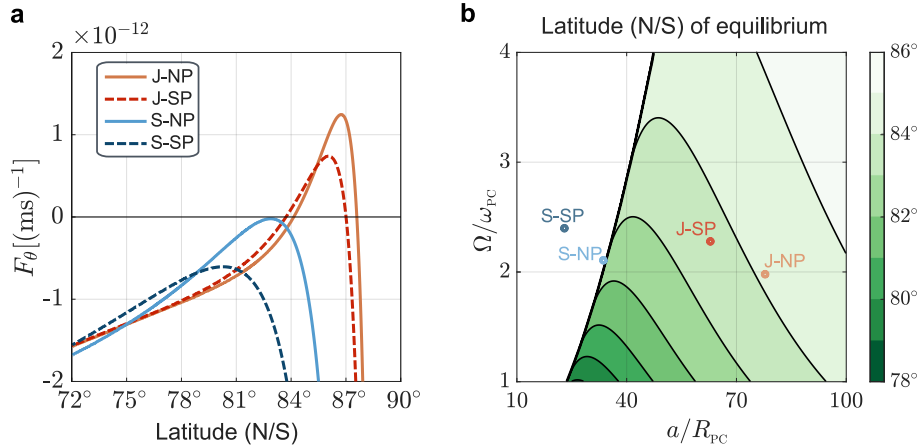


Figure 4: **Latitudes of equilibrium in the Gas Giants.** **a**, Curves of  $F_\theta$  as a function of latitude. The red curves are calculated for the north (solid) and south (dashed) poles of Jupiter (J-NP and J-SP, respectively); the blue curves represent the north (solid, S-NP) and south (dashed, S-SP) poles of Saturn. Only Jupiter has points of equilibrium in which  $F_\theta$  is zero. A stable balance for Jupiter’s poles is achieved at the equilibrium points farther from the pole. **b**, The latitude of equilibrium as a function of the ratio between the planetary radius ( $a$ ) and the radius of the PC ( $R_{\text{PC}}$ ), and of the ratio between the planetary rotation rate ( $\Omega$ ) and the rotation rate of the PC ( $\omega_{\text{PC}}$ ). Only the stable solutions for  $F_\theta = 0$  are considered. The white area on the left side of the contour is where equilibrium can not be achieved. The values representing the curves in **a** are shown as points. Both poles of Saturn are in the region with no solution.

of such equilibrium on Saturn, support the suggested mechanism as the stabilizing balance that holds the CPCs of Jupiter stable.

It can be seen (Fig. 4b) that the stable equilibrium is achieved farther from the poles when the PC rotates faster (smaller  $\Omega/\omega_{\text{PC}}$ ). This is because the vorticity gradient of the PC is proportional to its rotation rate, so faster rotating PCs can “overcome” the planetary vorticity gradient for greater distances from their centers. Larger polar vortices (smaller  $a/R_{\text{PC}}$ ) also result in farther latitudes of equilibrium. In this case, this is due to their vorticity gradient profiles being stretched farther. This, however, has a limitation. A PC too big, relative to the planet, will be in a state where its region of positive vorticity gradient is too far from the pole, where  $\beta$  dominates. In these cases, equilibrium cannot be reached, as is the case of the Saturnian poles.

### Zonal stability of circumpolar cyclones

Next, we investigate how many cyclones can fit in a circumpolar ring. All cyclones in the circumpolar ring are of nearly similar size and strength, with a comparable space between adjacent pairs<sup>4,5,6</sup>. Thus, in the following analysis, a ring of equally spaced identical cyclones is considered. Then, it is postulated that the cyclones are sustained by mutual rejection between their two neighboring vortices in the zonal direction, according to the force derived by their respective vorticity gradients (Fig. 5a). CPC2 is assumed to be exactly in the middle between CPCs 1 and 3, such that the zonal forces applied on it

are equal and opposite. The remaining question, however, is whether this equilibrium is stable. For understanding the stability criterion for a ring of CPCs, it is insightful to consider the second derivative in the zonal direction of the vorticity (only the vorticity induced by CPCs 1 and 3) at the center of CPC2, as a function of  $L$  (Fig. 5b). When  $L$  is too short, a small perturbation in the location of CPC2 to the left encounters a negative vorticity gradient (Fig. 5c), which pulls the vortex further to the left. The opposite happens with a perturbation to the right. This constitutes an unstable equilibrium that will exist as long as the second derivative of the vorticity is positive. When the second derivative of the vorticity is negative, a stable equilibrium is formed (Fig. 5d). The limiting distance,  $L_{\text{lim}} = 4.54R_{\text{CPC}}$  (Methods), in which the second derivative vanishes, is the minimal distance between CPCs that can maintain a stable equilibrium. This means that the vortex centers have to be more than  $L_{\text{lim}}$  apart in order for the CPCs to be in a sustainable configuration.

The available space for CPCs in the circumferential ring is approximately  $2\pi a(90^\circ - |\theta_{\text{eq}}|)\pi/180^\circ$ , where  $\theta_{\text{eq}}$  is the latitude of equilibrium for the respective pole (Fig. 4b). Therefore, the maximal number of vortices to fit in the ring can be estimated according to

$$N_{\text{max}} = \frac{2\pi a(90^\circ - |\theta_{\text{eq}}|)\pi/180^\circ}{4.54R_{\text{CPC}}}. \quad (2)$$

Here, values for  $R_{\text{CPC}}$  at the north and south poles of Jupiter are evaluated by Juno’s JIRAM imager<sup>5</sup>. Higher values inside the variability range of  $R_{\text{CPC}}$  were taken for the smallest

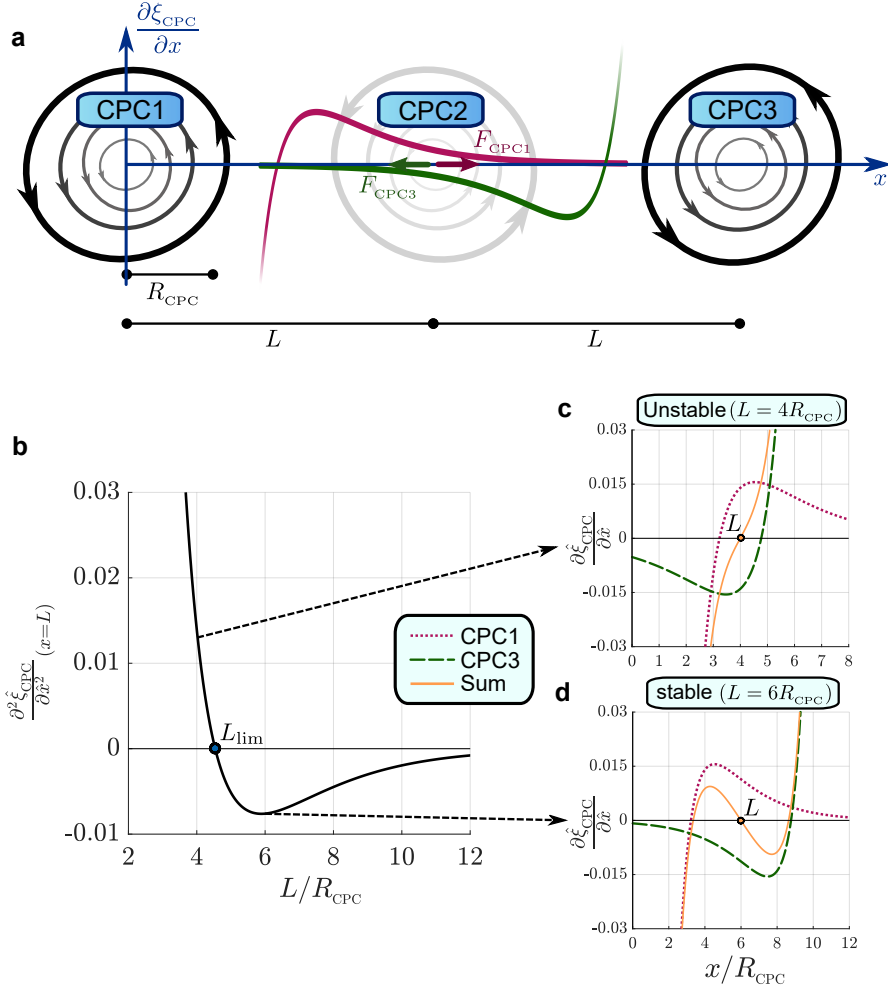


Figure 5: **Zonal stability of CPCs.** **a**, Schematic for the equilibrium between CPC2 and the adjacent vortices in the zonal direction, titled CPC1 and CPC3.  $x$  is the distance from CPC1 in the zonal direction. The radius of maximum velocity for a CPC is  $R_{\text{CPC}}$ . The distance between two neighboring cyclones is  $L$ .  $\xi_{\text{CPC}}$  is the vorticity profile produced by the presence of CPCs 1 and 3. The magenta and green curves are the vorticity gradients in the zonal direction induced by CPC1 and CPC3, respectively. The rejection force induced by each curve is illustrated as an arrow at the center of CPC2. **b**, The second derivative of  $\xi_{\text{CPC}}$  in the zonal direction, as a function of the distance  $L$ . This second derivative is evaluated at a distance  $L$  from CPC1. **c,d**, Plots representing an unstable and a stable case (respectively) of the vorticity gradient profiles as a function of  $x$ . **b-d**, For generalization of the plots, the hatted variables are non-dimensional (Methods).

constraint (Methods). Inserting the numbers for the north and south poles to equation (2) results in  $N \sim 11.05$  and  $\sim 7.26$ , respectively. However, as  $N$  should be an integer describing the maximal number of stable CPCs, these numbers are rounded down to give

$$N_{\text{max,N}} \sim 11, \quad N_{\text{max,S}} \sim 7, \quad (3)$$

where the subscripts N and S represent the north and south poles.

While this last analysis can be explained intuitively, to get a more accurate constraint, a 2D analysis is performed that does not treat CPC2 as a singular point but instead considers

the different influence, weighted by the meridional velocity of CPC2, around the spread of the vortex. The force acting on CPC2 by the presence of CPCs 1 and 3 is proportional<sup>22</sup> to the integral

$$F \sim \iint v_2(\xi_1 + \xi_3) dS \quad (4)$$

around CPC2. Here,  $v_2$  is the meridional velocity of CPC2, and  $\xi_{1(3)}$  is the vorticity of CPC1(3). The results from this analysis are qualitatively similar to those shown in Fig. 5; however, the limiting distance for stability ( $L_{\text{lim}}$ ) is found to be  $5.87R_{\text{CPC}}$  instead (Methods). This constrains  $N_{\text{max}}$  further as CPC2 is now influenced more by regions closer to CPCs

1 and 3. Using this value instead of  $4.54R_{\text{CPC}}$  in equation (2) results in  $N \sim 8.54$  and  $\sim 5.62$  for the north and south poles, such that

$$N_{\text{max,N}} \sim 8, \quad N_{\text{max,S}} \sim 5. \quad (5)$$

This constraint correctly predicts the actual number of vortices in the north and south poles of Jupiter. It is interesting to note that the estimation of  $N_{\text{max,S}}$  is in between 5 and 6, and, consistently, two years observations of the south pole found a constant gap in the south polar ring<sup>4</sup>, implying on space that is slightly larger than that required for the five CPCs. This gap was temporarily occupied with a sixth vortex around the time of Juno’s 18th perijove<sup>5</sup>, but as the formation was not stable, this additional vortex disappeared by the time of the 19th perijove, indicating that the 5.62 value has a dynamical meaning. These predictions further support the described mechanism for the stability of the CPCs on Jupiter.

### Polar cyclones on the Gas Giants

The analysis presented here is based on the assumption that large-scale movement of vortices is mainly due to advection of background vorticity with the tangential velocity of the vortex, and that this movement is proportional, both in magnitude and in direction, to the background vorticity gradient. This logic implies that if the background vorticity gradient is zero at the center of a vortex, that vortex will not move. The gradient of planetary vorticity that acts on a circumpolar cyclone in the meridional direction can be opposed under certain conditions by the gradient of vorticity induced by the polar cyclone (equation (1)). Such an equilibrium is shown (Fig. 4b) to be favored for small and strong PCs, relative to their host planets. In the zonal direction, it is shown (Fig. 5) that stability can be sustained for up to a certain amount of vortices in a circumpolar ring. More vortices can fit in the ring for poles in which the meridional stability is achieved at latitudes farther from the pole, and for poles with smaller CPCs. These analyses only treat the assumed highest-order forces that control the stability of circumpolar vortices, and suggest that the governing dynamics are controlled by 2D (barotropic) PV conservation. There are other forces, such as ones deriving from a 3D structure of a cyclone, that may be responsible for the small changes in the locations, speeds, and sizes observed in the circumpolar vortices of Jupiter<sup>4</sup>.

While this study explains the existence of circumpolar cyclones on Jupiter in contrast to the absence of such on Saturn, it does so by considering the specifics of their observed corresponding PCs. However, it does not explain the variation between the PCs of the planets. Theoretically, Saturn could sustain circumpolar vortices if its PCs were smaller or were to spin faster. Since the stability criterion for a circumpolar ring in the North Pole of Saturn is nearly reached, it may be that minor future variations in the polar conditions of Saturn (e.g., due to its seasonality) would manifest in a circumpolar ring or that such a ring existed in the past. It is also possi-

ble that cyclic variations in the solar forcing may alternate the number of circumpolar vortices between the north and south poles of Jupiter. Nonetheless, the match of the meridional and zonal force balances to the observations provides strong evidence that the physical balances outlined in this study are responsible for setting the location, stability, and number of circumpolar cyclones on the Gas Giants.

## Acknowledgments

We thank Keren Duer and Eli Galanti for insightful conversations. This research has been supported by the Minerva Foundation with funding from the Federal German Ministry for Education and Research and the Helen Kimmel Center for Planetary Science at the Weizmann Institute of Science.

## Author contributions

N.G. has designed the study, performed the calculations and written the paper with support of Y.K.

## Additional information

**Correspondence and requests for materials** should be addressed to N.G. (nimrod.gavriel@weizmann.ac.il)

## References

1. Bolton, S. J. *et al.* Jupiter’s interior and deep atmosphere: The initial pole-to-pole passes with the Juno spacecraft. *Science* **356**, 821–825 (2017).
2. Orton, G. S. *et al.* The first close-up images of Jupiter’s polar regions: Results from the Juno mission JunoCam instrument. *Geophys. Res. Lett.* **44**, 4599–4606 (2017).
3. Adriani, A. *et al.* Clusters of cyclones encircling Jupiter’s poles. *Nature* **555**, 216–219 (2018).
4. Tabataba-Vakili, F. *et al.* Long-term tracking of circumpolar cyclones on Jupiter from polar observations with JunoCam. *Icarus* **335**, 113405 (2020).
5. Adriani, A. *et al.* Two-year observations of the Jupiter polar regions by JIRAM on board Juno. *J. Geophys. Res. (Planets)* e2019JE006098 (2020).
6. Grassi, D. *et al.* First estimate of wind fields in the Jupiter polar regions from JIRAM-Juno images. *J. Geophys. Res. (Planets)* **123**, 1511–1524 (2018).
7. Fine, K., Cass, A., Flynn, W. & Driscoll, C. Relaxation of 2D turbulence to vortex crystals. *Phys. Rev. Lett.* **75**, 3277 (1995).
8. Schecter, D., Dubin, D., Fine, K. & Driscoll, C. Vortex crystals from 2D Euler flow: Experiment and simulation. *Phys. of Fluids*. **11**, 905–914 (1999).

9. Sayanagi, K. M., Blalock, J. J., Dyudina, U. A., Ewald, S. P. & Ingersoll, A. P. Cassini ISS observation of Saturn's north polar vortex and comparison to the south polar vortex. *Icarus* **285**, 68–82 (2017).
10. Showman, A. P., Ingersoll, A. P., Achterberg, R. & Kaspi, Y. The global atmospheric circulation of Saturn. *Saturn in the 21st Century* **20**, 295 (2018).
11. Kaspi, Y. *et al.* Comparison of the deep atmospheric dynamics of Jupiter and Saturn in light of the Juno and Cassini gravity measurements. *Space Sci. Rev.* **216**, 5, 84, 1–27 (2020).
12. Galanti, E. *et al.* Saturn's deep atmospheric flows revealed by the cassini grand finale gravity measurements. *Geophys. Res. Lett.* **46**, 616–624 (2019).
13. Baines, K. H. *et al.* Saturn's north polar cyclone and hexagon at depth revealed by Cassini/VIMS. *Planet. Space Sci.* **57**, 1671–1681 (2009).
14. Li, C., Ingersoll, A. P., Klipfel, A. P. & Brettle, H. Modeling the stability of polygonal patterns of vortices at the poles of Jupiter as revealed by the Juno spacecraft. *Proc. Natl. Acad. Sci. U.S.A.* **117**, 24082–24087 (2020).
15. Yadav, R. K., Heimpel, M. & Bloxham, J. Deep convection-driven vortex formation on Jupiter and Saturn. *Sci. Adv.* **6**, eabb9298 (2020).
16. Yadav, R. K. & Bloxham, J. Deep rotating convection generates the polar hexagon on Saturn. *Proc. Natl. Acad. Sci. U.S.A.* **117**, 13991–13996 (2020).
17. Garcia, F., Chambers, F. R. & Watts, A. L. Deep model simulation of polar vortices in gas giant atmospheres. *Mon. Not. Roy. Astro. Soc.* **499**, 4698–4715 (2020).
18. Afanasyev, Y. & Zhang, Y. Cyclonic circulation of Saturn's atmosphere due to tilted convection. *Nature Geoscience* **11**, 164–167 (2018).
19. Afanasyev, Y. & Huang, Y.-C. Poleward translation of vortices due to deep thermal convection on a rotating planet. *Geophys. Astrophys. Fluid Dyn.* **114**, 821–834 (2020).
20. Aubert, O., Le Bars, M., Le Gal, P. & Marcus, P. S. The universal aspect ratio of vortices in rotating stratified flows: experiments and observations. *J. Comp. Phys.* **706**, 34–45 (2012).
21. Lemasquerier, D., Facchini, G., Favier, B. & Le Bars, M. Remote determination of the shape of Jupiter's vortices from laboratory experiments. *Nature Physics* **16**, 695–700 (2020).
22. Rossby, C. On displacements and intensity changes of atmospheric vortices. *J. Mar. Res.* **7**, 71 (1948).
23. Adem, J. A series solution for the barotropic vorticity equation and its application in the study of atmospheric vortices. *Tellus* **8**, 364–372 (1956).
24. Smith, R. K., Ulrich, W. & Dietachmayer, G. A numerical study of tropical cyclone motion using a barotropic model. I: The role of vortex asymmetries. *Q. J. R. Meteorol. Soc.* **116**, 337–362 (1990).
25. Shapiro, L. J. Hurricane vortex motion and evolution in a three-layer model. *J. Atmos. Sci.* **49**, 140–154 (1992).
26. Smith, R. B. A hurricane beta-drift law. *J. Atmos. Sci.* **50**, 3213–3215 (1993).
27. Franklin, J. L., Feuer, S. E., Kaplan, J. & Aberson, S. D. Tropical cyclone motion and surrounding flow relationships: Searching for beta gyres in omega dropwindsonde datasets. *Mon. Weath. Rev.* **124**, 64–84 (1996).
28. Chan, J. C. The physics of tropical cyclone motion. *Ann. Rev. Fluid Mech.* **37**, 99–128 (2005).
29. O'Neill, M. E., Emanuel, K. A. & Flierl, G. R. Polar vortex formation in giant-planet atmospheres due to moist convection. *Nature Geoscience* **8**, 523–526 (2015).
30. O'Neill, M. E., Emanuel, K. A. & Flierl, G. R. Weak jets and strong cyclones: Shallow-water modeling of giant planet polar caps. *J. Atmos. Sci.* **73**, 1841–1855 (2016).
31. Scott, R. Polar accumulation of cyclonic vorticity. *Geophys. Astrophys. Fluid Dyn.* **105**, 409–420 (2011).
32. Brueshaber, S. R., Sayanagi, K. M. & Dowling, T. E. Dynamical regimes of giant planet polar vortices. *Icarus* **323**, 46–61 (2019).
33. Zhao, H., Wu, L. & Zhou, W. Observational relationship of climatologic beta drift with large-scale environmental flows. *Geophys. Res. Lett.* **36** (2009).
34. Rivière, G., Arbogast, P., Lapeyre, G. & Maynard, K. A potential vorticity perspective on the motion of a mid-latitude winter storm. *Geophys. Res. Lett.* **39** (2012).
35. Fiorino, M. & Elsberry, R. L. Some aspects of vortex structure related to tropical cyclone motion. *J. Atmos. Sci.* **46**, 975–990 (1989).
36. Sutyrin, G. G. & Flierl, G. R. Intense vortex motion on the beta plane: Development of the beta gyres. *J. Atmos. Sci.* **51**, 773–790 (1994).
37. Vallis, G. K. *Atmospheric and oceanic fluid dynamics* (Cambridge University Press, 2017).

## Methods

**Idealized cyclone profiles.** The observed velocity profiles for the vortices at the poles of Jupiter<sup>6</sup> are very similar to a solid-disk rotation in an inner region and an exponential decay outside of it (Extended Data Fig. 1). This behavior is expressed by an idealized cyclone tangential velocity profile given as

$$v_{\text{PC}} = \begin{cases} V \frac{r}{R} & 0 \leq r < R \\ V e^{-\frac{r-R}{2R}} & r \geq R \end{cases}, \quad (6)$$

where  $r$  is the distance from the center of the cyclone,  $V$  is the maximum velocity in the vortex, and  $R$  is the edge of the solid disk. This profile is compared in Extended Data Fig. 3a with a profile suggested for a study of tropical cyclones<sup>24</sup> and with a profile fit specifically for the PCs of Jupiter<sup>6</sup>. This velocity profile (equation (6)) is also compared with wind measurements from Jupiter and Saturn in Extended Data Figs. 1 and 2, respectively. The stronger decay of velocity around 3,000 km at the Jovian poles (Extended Data Fig. 1) can be attributed to the presence of the velocity fields of the CPCs, as no such trend appears in the PC only cases of the Saturnian poles (Extended Data Fig. 2). The relative vorticity around the center of the cyclone is calculated for a cyclone put in a medium otherwise at rest as  $\xi = \frac{1}{r} \frac{\partial(rv_{\text{PC}})}{\partial r}$  to give

$$\xi_{\text{PC}} = \begin{cases} 2 \frac{V}{R} & 0 \leq r < R \\ \left(\frac{R}{r} - \frac{1}{2}\right) \frac{V}{R} e^{-\frac{r-R}{2R}} & r \geq R \end{cases}. \quad (7)$$

This profile is compared with the vorticity calculated from the two other velocity profiles in Extended Data Fig. 3b. The vorticity gradient is thus

$$\frac{\partial \xi_{\text{PC}}}{\partial r} = \begin{cases} 0 & 0 \leq r < R \\ \frac{V}{R^2} e^{-\frac{r-R}{2R}} \left(\frac{1}{4} - \frac{R}{2r} - \frac{R^2}{r^2}\right) & r \geq R \end{cases}. \quad (8)$$

This profile is again compared with the two other profiles in Extended Data Fig. 3c. The velocity profile from the numerical study<sup>24</sup> is an inverse high order polynomial. This means that the second derivative of this velocity profile, which is the requested term, is very noisy. On the other hand, the curve fit for J-NP<sup>6</sup> is only suited for a small range of  $r$  and shows a large vorticity gradient near  $r = R$  that is an artifact of the chosen curve. For these reasons, we chose to perform the calculations of this study with the suggested piece-wise profile (equations (6)-(8)).

**Equations for the meridional stability** The planetary background vorticity ( $f$ ) is

$$f = 2\Omega \cos(r/a), \quad (9)$$

where  $\Omega$  is the planetary rotation rate, and  $a$  is the radius of the planet. The planetary vorticity gradient is

$$\beta \equiv \frac{\partial f}{\partial r} = -2\Omega a^{-1} \sin(r/a). \quad (10)$$

In order to show Fig. 4 in terms of latitude, the transformation  $r = a(90^\circ - \theta)\pi/180^\circ$  is used in equation (1). The two terms in equation (1) are defined by equation (8) and equation (10). For the planetary rotation rates ( $\Omega$ ), the values  $1.76 \times 10^{-4}$  and  $1.65 \times 10^{-4} \text{ s}^{-1}$  are used for Jupiter and Saturn, respectively. The mean planetary radii ( $a$ ) used here are 69,911 km for Jupiter and 58,232 km for Saturn. Maximum velocities ( $V$ ) and radii of maximum velocity ( $R = R_{\text{PC}}$ ) are estimated for Jupiter (Grassi et al., 2018<sup>6</sup>, Fig. 6) and Saturn (Baines et al., 2009<sup>13</sup>, Tab. 2) from observations. For J-NP, J-SP, S-NP, and S-SP, those values are  $V = \{80, 85, 136, 174\} \text{ ms}^{-1}$  and  $R_{\text{PC}} = \{900, 1100, 1728, 2541\} \text{ km}$ , respectively.

In Fig. 4b, the contour shows the solutions  $\theta_{\text{eq}}$  for  $F_\theta = 0$ , reduced to

$$\theta_{\text{eq}} = G(a/R_{\text{PC}}, \Omega/\omega_{\text{PC}}), \quad (11)$$

where  $G$  is a function defined by using equation (8) and equation (10), and  $\omega_{\text{PC}} = V/R_{\text{PC}}$  is the rotation rate of the solid-disk part of the PC. While at some range of  $a/R_{\text{PC}}$  and  $\Omega/\omega_{\text{PC}}$  there is no solution, as can be seen in Fig. 4b, for the rest of the range, there are two possible solutions. Only the stable solutions (where  $\left. \frac{\partial F_\theta}{\partial \theta} \right|_{\theta=\theta_{\text{eq}}} > 0$ ) are taken for Fig. 4b.



**Equations for zonal stability** For plotting the general trends in Fig. 5, equation (8) (for the CPC, in the zonal direction) is normalized according to

$$r = \hat{x}R_{\text{CPC}}, \quad \xi = \hat{\xi}V_{\text{CPC}}/R_{\text{CPC}}, \quad (12)$$

where variables with a circumflex are non-dimensional,  $\hat{x}$  is the non-dimensional distance from the center of CPC1 in the eastward direction,  $R_{\text{CPC}}$  is the radius of maximum velocity of the CPCs, and  $V_{\text{CPC}}$  is the maximum velocity of the CPCs. These scalings result in equation (8) becoming

$$\frac{\partial \hat{\xi}}{\partial \hat{x}} = \begin{cases} 0 & 0 \leq \hat{x} < 1 \\ e^{-\frac{\hat{x}-1}{2}} \left( \frac{1}{4} - \frac{1}{2\hat{x}} - \frac{1}{\hat{x}^2} \right) & \hat{x} \geq 1 \end{cases}. \quad (13)$$

The total vorticity gradient in the zonal direction, felt on CPC2 by CPCs 1 and 3, is therefore

$$\frac{\partial \hat{\xi}_{\text{CPC2}}}{\partial \hat{x}} = \frac{\partial \hat{\xi}}{\partial \hat{x}} - \left[ \frac{\partial \hat{\xi}}{\partial \hat{x}} \right]_{\hat{x} \rightarrow (2L/R_{\text{CPC}} - \hat{x})}. \quad (14)$$

In Fig. 5b, the expression  $\left[ \frac{\partial}{\partial \hat{x}} \left( \frac{\partial \hat{\xi}_{\text{CPC2}}}{\partial \hat{x}} \right) \right]_{\hat{x} \rightarrow L/R_{\text{CPC}}}$  is plotted against  $L/R_{\text{CPC}}$ . The minimum distance between CPCs required for stability ( $L_{\text{lim}}$ ) is the solution  $L$  for the equation

$$\left[ \frac{\partial}{\partial \hat{x}} \left( \frac{\partial \hat{\xi}_{\text{CPC2}}}{\partial \hat{x}} \right) \right]_{\hat{x} \rightarrow L/R_{\text{CPC}}} = 0. \quad (15)$$

This value is found to be  $L_{\text{lim}} = 4.54R_{\text{CPC}}$ . In Fig. 5c-d, equation (14) is plotted against  $\hat{x}$  for two different values of  $L$ . In Fig. 5c,  $L$  is smaller than  $L_{\text{lim}}$ , illustrating an unstable equilibrium that would result in a merger with either CPC1 or 3. In Fig. 5d,  $L$  is larger than  $L_{\text{lim}}$ , and the equilibrium is stable.

For solving equation (2),  $R_{\text{CPC}}$  is evaluated according to  $R_{\text{CPC}} = R_{\text{PC}}R_{\text{ratio}}^{-1}$ , where the ratios between the radii of the PC and the CPCs ( $R_{\text{ratio}}$ ) are estimated from Adriani et al. 2020<sup>5</sup> (Fig. 5b). We used the minimal (for most restrictive constraint) observed values of  $R_{\text{ratio}} = 1$  for J-NP, and  $R_{\text{ratio}} = 0.75$  for J-SP. Values for  $R_{\text{PC}}$  are the same as for the meridional analysis. For  $|\theta_{\text{eq}}|$ , the values  $84.1^\circ$  and  $83.7^\circ$  found from Fig. 4 for J-NP and J-SP, respectively, were used. The resulting  $N_{\text{max}}$  was rounded down, as rounding up would result in an unstable amount of CPCs.

**Accurate estimation of  $L_{\text{lim}}$**  For a more accurate prediction of the limiting distance between vortices for stability, a 2D analysis is done instead of the 1D analysis done for Fig. 5. We use here the notion that the vorticity gradient force is proportional to the integral shown in equation (4). Stability is achieved when this force is positive (pushes right) when the position of CPC2 is perturbed to the left and is negative when this position is perturbed to the right. Therefore, the limiting  $L$  for stability ( $L_{\text{lim}}$ ) is the value of  $L$  in which the gradient of the force with respect to the location of CPC2 vanishes.

For performing the integration in equation (4), the ideal profiles (equations (6) and (7)) are converted to a Cartesian coordinate system. This gives (in normalized variables according to equation (12), where  $v = \hat{v}V_{\text{CPC}}$ )

$$\begin{aligned} \hat{v}_2 &= \begin{cases} r_2 \cos(\phi) & 0 \leq r_2 < 1 \\ e^{-\frac{r_2-1}{2}} \cos(\phi) & r_2 \geq 1 \end{cases}, \\ \hat{\xi}_1 &= \begin{cases} 2 & 0 \leq r_1 < 1 \\ \left( \frac{1}{r_1} - \frac{1}{2} \right) e^{-\frac{r_1-1}{2}} & r_1 \geq 1 \end{cases}, \\ \hat{\xi}_3 &= \begin{cases} 2 & 0 \leq r_3 < 1 \\ \left( \frac{1}{r_3} - \frac{1}{2} \right) e^{-\frac{r_3-1}{2}} & r_3 \geq 1 \end{cases}, \end{aligned} \quad (16)$$

where

$$\begin{aligned} \hat{r}_1 &= \sqrt{\hat{x}^2 + \hat{y}^2}, \\ \hat{r}_2 &= \sqrt{(\hat{x} - \hat{x}_2)^2 + \hat{y}^2}, \\ \hat{r}_3 &= \sqrt{(\hat{x} - 2L/R_{\text{CPC}})^2 + \hat{y}^2}, \\ \phi &= \tan^{-1} \left( \frac{\hat{y}}{\hat{x} - \hat{x}_2} \right), \end{aligned} \quad (17)$$

$\hat{x}_2$  is the normalized (by  $R_{\text{CPC}}$ ) distance between the centers of CPC1 and CPC2, and  $\hat{y}$  is the northward meridional distance from the center of CPC1, normalized by  $R_{\text{CPC}}$ .  $L_{\text{lim}}$  is then the value of  $L$  that solves the equation

$$\left[ \frac{\partial}{\partial \hat{x}_2} \left( \iint \hat{v}_2 (\hat{\xi}_1 + \hat{\xi}_3) dS \right) \right]_{\hat{x}_2=L/R_{\text{CPC}}} = 0. \quad (18)$$

For validation, the domain of integration is determined to be very small, in which case the resulting  $L_{\text{lim}}$  approached the value from the 1D analysis ( $4.54R_{\text{CPC}}$ ). The domain of integration is ultimately chosen to be  $\{\hat{x}_2 - (L/R_{\text{CPC}} - 2), \hat{x}_2 + (L/R_{\text{CPC}} - 2)\}$  for  $\hat{x}$ , and  $\{-(L/R_{\text{CPC}} - 2), (L/R_{\text{CPC}} - 2)\}$  for  $\hat{y}$ . This way, the resulting force is not stemming from the predominant areas of CPCs 1 and 3. The solution  $L_{\text{lim}}$  to equation (18) is thus  $L_{\text{lim}} = 5.87$ .

**Formal asymptotic derivation of the suggested balance on the CPCs: momentum balance approach** In order to show how the described balance suggested in this study results from the equations of motion, an asymptotic derivation is laid out. First, a time scale that is long enough to describe the changes in the CPCs is needed. This time-scale is derived here from the vorticity equation by balancing between the vorticity change with time and the  $\beta$  term, as this term is assumed to be a substantial contributor to the motion of Jovian cyclones. Thus, it follows that

$$\frac{\partial \xi}{\partial t} \propto \beta v, \quad (19)$$

leading to the scaling argument

$$T \propto \frac{1}{\beta L} \approx 11 [\text{days}], \quad (20)$$

where Jovian values were assumed,  $\beta$  was estimated at latitude  $84^\circ$  (near the center of the CPCs), and  $L \approx 2000$  km was estimated according to the observed radii of the CPCs. This time scale is of the same order as the time between perijoves ( $\sim 53$  days), in which slight variations can be observed in the locations and sizes of the CPCs<sup>5,4</sup>. To continue, we assume that the flow is 2D, inviscid, and barotropic. We start from the horizontal conservation of momentum equation<sup>37</sup> in the form

$$\frac{\partial \mathbf{u}}{\partial t} + (f + \xi) \hat{k} \times \mathbf{u} = -\frac{1}{\rho} \nabla p - \frac{1}{2} \nabla (\mathbf{u}^2), \quad (21)$$

where  $p$  is pressure and  $\mathbf{u}$  is the velocity vector. We scale and expand the variables at the core of a CPC according to

$$\begin{aligned} x = L\hat{x}, \quad y = L\hat{y}, \quad t = (\beta L)^{-1} \hat{t}, \quad u = U(\hat{u}_{\text{CPC}} + \text{Ro} \hat{u}_{\text{PC}}), \quad v = U(\hat{v}_{\text{CPC}} + \text{Ro} \hat{v}_{\text{PC}}), \\ p = f_0 U L \rho (\hat{p}_{\text{CPC}} + \text{Ro} \hat{p}_{\text{PC}}), \quad f = (f_0 + \beta L \hat{y}), \quad \xi = \frac{U}{L} (\hat{\xi}_{\text{CPC}} + \text{Ro} \hat{\xi}_{\text{PC}}). \end{aligned} \quad (22)$$

Here,  $\text{Ro}$  is the Rossby number, taken as the small asymptotic expansion constant ( $\text{Ro} = \frac{U}{f_0 L} \approx 0.05$ ), where  $U$  is the velocity scale ( $\sim 40 \text{ms}^{-1}$ ), and  $f_0$  is evaluated at latitude  $84^\circ$ . The velocities (and therefore the pressure and vorticity as well) due to the PCs are assumed to be  $O(\text{Ro})$  smaller than those of the CPC since the PC is far when looking at the core of a CPC. The pressure here is scaled according to geostrophic balance. Note that here the meridional direction is northward ( $y$ ) and not equatorward ( $r$ ) as defined in the main text. This expansion results in

$$\begin{aligned} \frac{\beta L}{f_0} \left( \frac{\partial \hat{\mathbf{u}}_{\text{CPC}}}{\partial \hat{t}} \right) + \left( 1 + \frac{\beta L}{f_0} \hat{y} + \text{Ro} \left( \hat{\xi}_{\text{CPC}} + \text{Ro} \hat{\xi}_{\text{PC}} \right) \right) \hat{k} \times (\hat{\mathbf{u}}_{\text{CPC}} + \text{Ro} \hat{\mathbf{u}}_{\text{PC}}) \\ = -\nabla (\hat{p}_{\text{CPC}} + \text{Ro} \hat{p}_{\text{PC}}) - \text{Ro} \frac{1}{2} \nabla (\hat{\mathbf{u}}_{\text{CPC}} \cdot \hat{\mathbf{u}}_{\text{CPC}} + 2\text{Ro} \hat{\mathbf{u}}_{\text{PC}} \cdot \hat{\mathbf{u}}_{\text{CPC}} + O(\text{Ro}^2)), \end{aligned} \quad (23)$$

where  $\hat{k}$  is a unit vector in the vertical direction. The non-dimensional number  $\frac{\beta L}{f_0}$  is evaluated at latitude  $84^\circ$  as  $\sim 0.003$ , which is  $O(\text{Ro}^2)$ . In the leading order we have (back in dimensional variables) a geostrophic balance on the CPC

$$f_0 \hat{k} \times \mathbf{u}_{\text{CPC}} = -\frac{1}{\rho} \nabla p_{\text{CPC}}. \quad (24)$$

For the second order we get a modified geostrophic balance for the PC

$$f_0 \hat{k} \times \mathbf{u}_{\text{PC}} = -\frac{1}{\rho} \nabla p_{\text{PC}} - \xi_{\text{CPC}} \hat{k} \times \mathbf{u}_{\text{CPC}} - \nabla (\mathbf{u}_{\text{CPC}} \cdot \mathbf{u}_{\text{CPC}}). \quad (25)$$

For the third order, where the time evolution appears, we have

$$\frac{\partial \mathbf{u}_{\text{CPC}}}{\partial t} + (\beta y + \xi_{\text{PC}}) \hat{k} \times \mathbf{u}_{\text{CPC}} + \xi_{\text{CPC}} \hat{k} \times \mathbf{u}_{\text{PC}} = -\nabla (\mathbf{u}_{\text{PC}} \cdot \mathbf{u}_{\text{CPC}}). \quad (26)$$

Expanding equation (26) in the meridional direction, while using equation (24), gives

$$\frac{\partial v_{\text{CPC}}}{\partial t} + u_{\text{CPC}} (\xi_{\text{PC}} + \beta y) = -\frac{1}{f_0 \rho} \frac{\partial}{\partial y} \left( \frac{\partial p_{\text{CPC}}}{\partial x} u_{\text{PC}} \right) - v_{\text{CPC}} \frac{\partial v_{\text{PC}}}{\partial y} - v_{\text{PC}} \frac{\partial v_{\text{CPC}}}{\partial y}. \quad (27)$$

Since the PC terms are zonally symmetric, and since the CPC terms on the right-hand side are anti-symmetric in the zonal direction relative to the core of the CPC, a concentric integration of equation (27) around the core of the CPC results in the vanishing of all the terms on the right-hand side. Therefore, we get that

$$F_y = - \iint u_{\text{CPC}} (\xi_{\text{PC}} + \beta y) dS, \quad (28)$$

where  $F_y$  is the meridional force density on the CPC core. By considering the anti-symmetry of  $u_{\text{CPC}}$  in the meridional direction, one can show that  $F_y$  vanishes only when  $\iint \frac{\partial}{\partial y} (\xi_{\text{PC}} + \beta y) dS = 0$ , resulting in the condition  $F_\theta = 0$  (equation (1)). Taking the zonal direction of equation (26), and replacing the velocities according to Fig. 5 would similarly result in

$$F_x = \iint v_{\text{CPC}2} (\xi_{\text{CPC}1} + \xi_{\text{CPC}3}) dS. \quad (29)$$

**Formal asymptotic derivation of the suggested balance on the CPCs: vorticity balance approach** Another way to arrive at the condition  $F_\theta = 0$  (equation (1)) is to look at the vorticity equation. Taking the curl of equation (24) gives

$$\nabla \cdot \mathbf{u}_{\text{CPC}} = 0. \quad (30)$$

Taking the curl of equation (25) gives

$$(\mathbf{u}_{\text{CPC}} \cdot \nabla) \xi_{\text{CPC}} + f_0 (\nabla \cdot \mathbf{u}_{\text{PC}}) = 0. \quad (31)$$

Assuming that the core of the CPC rotates, in equilibrium, as a solid body ( $\frac{\partial \xi_{\text{CPC}}}{\partial x} = \frac{\partial \xi_{\text{CPC}}}{\partial y} = 0$ ) gives that

$$\nabla \cdot \mathbf{u}_{\text{PC}} = 0. \quad (32)$$

Taking the curl of equation (26) gives

$$\frac{\partial \xi_{\text{CPC}}}{\partial t} + v_{\text{CPC}} \left( \frac{\partial \xi_{\text{PC}}}{\partial y} + \beta \right) + (\xi_{\text{PC}} + \beta y) (\nabla \cdot \mathbf{u}_{\text{CPC}}) + \xi_{\text{CPC}} (\nabla \cdot \mathbf{u}_{\text{PC}}) + (\mathbf{u}_{\text{PC}} \cdot \nabla) \xi_{\text{CPC}} + \frac{\partial \xi_{\text{PC}}}{\partial x} u_{\text{CPC}} = 0. \quad (33)$$

Using the solid-body rotation assumption again, together with equations (30) and (32), and noting that  $\xi_{\text{PC}}$  is zonally symmetric gives

$$\frac{\partial \xi_{\text{CPC}}}{\partial t} = -v_{\text{CPC}} \left( \frac{\partial \xi_{\text{PC}}}{\partial y} + \beta \right), \quad (34)$$

where the term in the parentheses can be regarded as  $\frac{\partial \omega}{\partial y}$  in Fig. 2. As  $v_{\text{CPC}}$  is anti-symmetric in the zonal direction, two opposite vorticity anomalies can be generated in the two sides of the CPC core when  $\frac{\partial \omega}{\partial y} \neq 0$ , resulting in a net meridional acceleration on the core.

## Data Availability

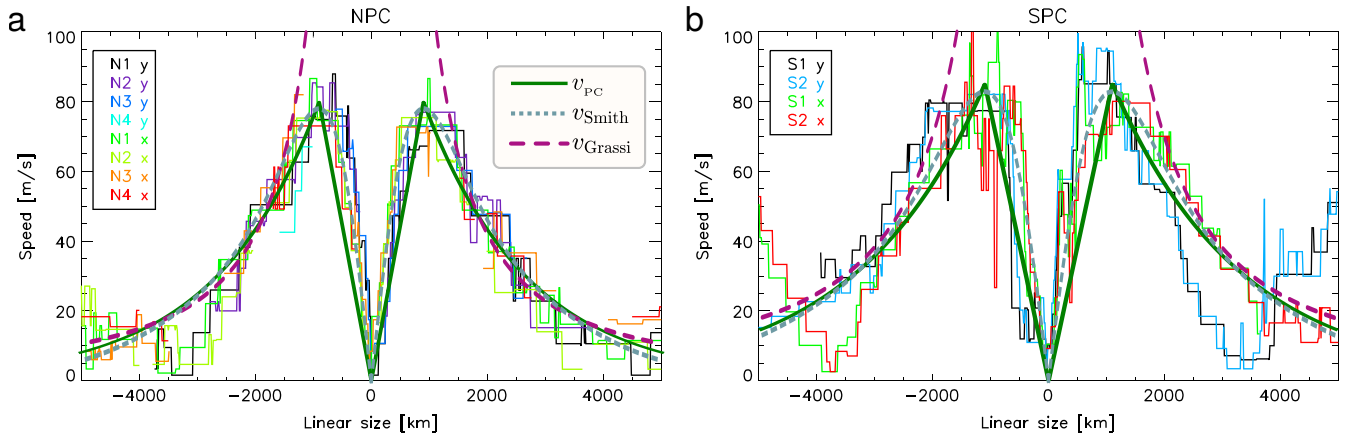
No data sets were generated or analyzed during the current study.

## Code availability

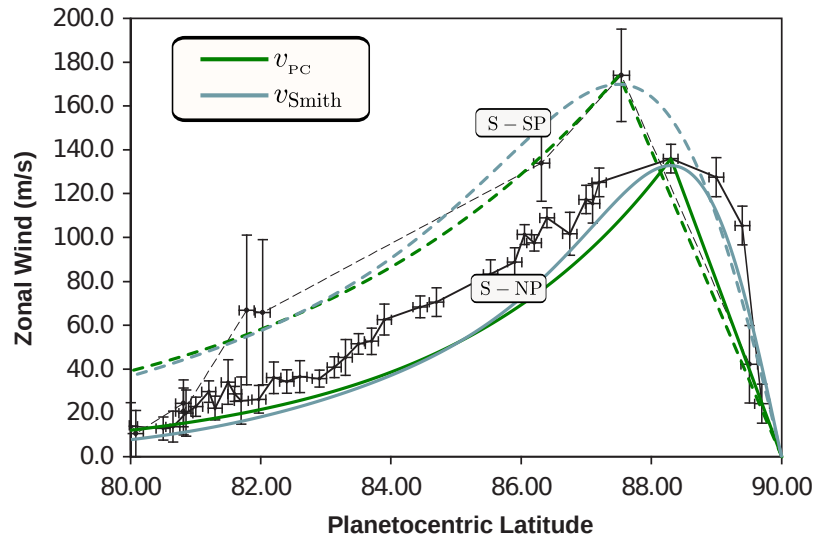
The MATLAB codes used for calculating and plotting the figures in this paper are available on request from N.G.

## Competing interests

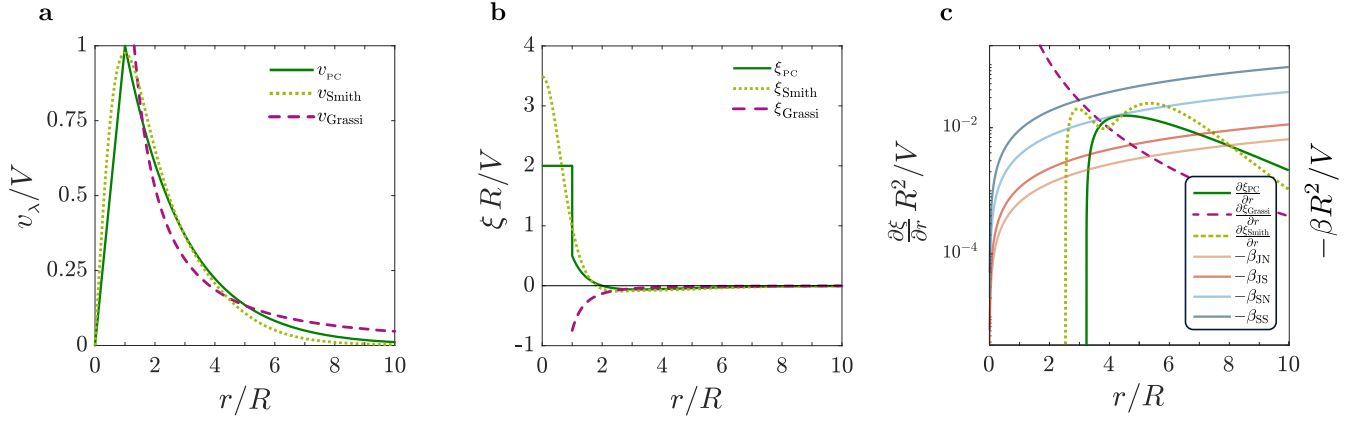
The authors declare no competing interests.



Extended Data Fig. 1: **Measurements of the Jovian PC velocity profiles.** The velocity profiles from Extended Data Fig. 3a, overlaid on Fig. 6 from Grassi et al., 2018<sup>6</sup> (adapted with permission), showing the observed velocities around the north (a) and south (b) poles of Jupiter. The idealized velocity profiles were calculated using the Jovian values for  $R$  and  $V$  (Methods). The green curves ( $v_{PC}$ ) represent the velocity profiles used for the analyses in this study.



Extended Data Fig. 2: **Measurements of the Saturnian PC velocity profiles.** Two velocity profiles from Extended Data Fig. 3a, overlaid on Fig. 8 from Baines et al., 2009<sup>13</sup> (adapted with permission), showing the observed velocities around the north (solid) and south (dashed) poles of Saturn. Error bars are calculated as standard deviations<sup>13</sup>. The idealized velocity profiles were calculated using the Saturnian values for  $R$  and  $V$  (Methods). The green curves ( $v_{PC}$ ) represent the velocity profiles used for the analyses in this study.



Extended Data Fig. 3: **Idealized profiles of velocity, vorticity, and vorticity gradient.** **a**, The vortex velocity profile according to the suggested piece-wise function (green solid curve) from equation (6) compared with two other ideal vortex profiles<sup>24,6</sup> (for the Grassi curve<sup>6</sup>,  $\gamma = 1.5$  was taken). **b**, The vorticity calculated for the same profiles as **a**. **c**, Vorticity gradient (in log scale), calculated for the same three profiles. In addition, the minus of the  $\beta$  profiles are shown for the northern and southern poles of Saturn and Jupiter. The 4 curves for  $-\beta$  differentiate as the vorticity gradient is normalized according to each polar cyclone, and as the length is scaled by the radius of maximum velocity for the respective PC. The points where the vorticity gradient curves cross the  $-\beta$  curves represent equilibrium. Here, 0 in the  $r/R$  axis represents the pole.